Electrodeposition of Ni-Co alloys from neat protic ionic liquid: Application to the hydrogen evolution reaction

Yuelin Xie, Antoine Miche, Vincent Vivier, Mireille Turmine

Electrodeposition of Ni-Co Alloys from Neat Protic Ionic Liquid: Application to the Hydrogen Evolution Reaction

Yuelin Xie, Antoine Miche, Vincent Vivier, Mireille Turmine*

[a] Sorbonne Université, CNRS, Laboratoire de Réactivité de Surface (LRS), 4 Place Jussieu, F-75005, Paris, France

Keywords: Protic ionic liquid, Electrodeposition, Amorphous alloys, Ni-based alloys, Hydrogen evolution reaction

* *Corresponding author: mireille.turmine@sorbonne-universite.fr*

Abstract

Amorphous and nanocrystalline Ni-Co alloys have been deposited on FTO glass in ethylammonium nitrate (EAN), a protic ionic liquid (PIL). The physicochemical properties of EAN with Ni^{2+} and Co^{2+} salts have been studied as well as the electrochemical behavior of these metal cations in the PIL in aerated atmosphere. Electrochemical studies showed that the redox reactions of Ni^{2+} and Co^{2+} leading to metal deposit on glassy carbon are not reversible in those conditions due to the formation of an oxide film. Conversely, when electrodeposition of Co, Ni and Ni-Co alloys on FTO glass in EAN was performed at 60°C in an oxygen-free environment, nanocrystalline Ni-Co alloys with different atomic ratios were obtained depending on both the deposition potential and ion concentration in solution. The composition and the morphology of the electroplated alloys were determined by several techniques such as SEM, TEM, XRD and XPS. The electrocatalytic properties of these materials were investigated towards the hydrogen evolution reaction (HER). It was shown that the addition of Co in Ni-based alloys can promote the HER, and most notably, amorphous Ni-Co alloys shows lower overpotential or reaction rate. Up to now, the better electrocatalytic results were obtained with the amorphous $Ni_{51.9}Co_{48.1}$ alloy, electrodeposited in EAN at high potential (-1.3 V/Ag/Ag^+). This work provides a new route to prepare nanocrystalline and amorphous Ni-Co alloys with different ratio in PIL

for practical applications in electrocatalysis such as water splitting.

1.Introduction

Water splitting is considered to be one of the most efficiency ways for the hydrogen evolution reaction (HER) as a potential of low-carbon energy source. To achieve this goal, research on the preparation of electrocatalysts has received an increasing interest in recent years, and more effective catalysts have been studied. As it has already been well established, precious metals such as platinum and palladium, always show excellent performance for water splitting electrolysis, resulting in low overpotential or fast reaction rate [1]. However, the scarcity cost is a barrier to their use in HER as well as other electrochemical reaction of interest such as the oxygen evolution reaction (OER). To address this problem, transition metal-based electrocatalysts are considered as alternative to replace these noble metals, especially for HER, due to the similar free energy of the hydrogen, ΔG_{H^*} [2].

Adjusting the electron structure of transition metal-based materials by using alloying is one of the approaches being considered. Since the first investigations of the HER mechanism on metallic Ni-Co in the 1960s, extensive research has been performed to develop the preparation and application of transition metal alloys [3, 4]. Different combinations of metal elements were investigated in previous works, such as Ni-Mo, Ni-Co, Ni-Al, Co-Mo, Co-Fe, and Fe-P [5-10]. In addition to modifying composition and morphology of transition metal alloys, adjusting the crystal structure is another way to improve HER performance. Amorphous alloys show characteristic in structural heterogeneities and high atomic diffusion rate resulting in great properties for chemical applications, especially in catalysis, due to their metastable structure and higher energy state [11-15]. Interestingly, electrodeposition is a possible route for the preparation of such alloys. For instance, Han et al.[16] prepared amorphous Ni-Mo alloy by pulse

plating technique. They showed that the addition of 30 wt.% Mo, leads to a decrease in overpotential of 62 mV for a current density of -0.2 $A \cdot cm^{-2}$ at 80°C. Similarly, amorphous Ni-Fe-Co-P alloy prepared by Bachvarov et al.[17] showed a decrease of overpotential by 89 mV than for crystalline Ni-Fe-Co alloy.

Although crystalline alloys do not generally perform as well as amorphous ones, nanocrystalline alloys have been studied in recent years showing excellent properties for water splitting applications [18-21]. However, it remains to be established whether the amorphous or nanocrystalline alloy is the best.

Many methods have been considered to synthesize transition metal alloys for electrocatalytic HER, such as sintering [22], pulsed layer deposition [23, 24], sol-gel [25], and electrodeposition [3, 26-31]. Among these techniques, electrodeposition has the advantage of fewer steps, ease of implementation and control, making it a versatile method for large-scale applications. Ahn et al. [27] have prepared Ni dendrites by electrodeposition on glassy carbon for HER in alkaline water electrolyte. The stability of HER was maintained without significant variation in overpotential for 2000 cycles. Nanoscale nickel electrodeposited on a Ni substrate by Zhou et al. shows higher current density than regular Ni-modified substrate with the same overpotential [32]. Recently, nanostructured Ni-Co alloys with different morphologies were electrodeposited in water showing an improvement of the electrocatalytic activity [4, 19, 33-35]. However, the unavoidable presence of water in the electrodeposition electrolyte can lead to undesirable hydrolysis of the organic media and creates unwanted compounds. This can be circumvented by using ionic liquids (ILs) which are more and more used as electrolyte for electrodeposition because of their large electrochemical window, high ionic conductivity, and simplicity of handling due to their non-volatility and inflammability. Nanocrystals can be electrodeposited from ILs more easily than in

aqueous solutions [36]. Additionally, as ILs can be divided into two families, aprotic ionic liquids (AILs) and protic ionic liquids (PILs), they offer a wide range of possible combinations between anions and cations. In earlier studies, although AILs have been more prevalent than PILs for electrodeposition applications, the latter have the advantage of easier synthesis. They also usually show lower viscosity and higher conductivity than AILs [37]. In recent years, the use of PILs in electrodeposition has been increasingly studied. As shown for instance in the case of zinc electrodeposition in 1-methylimidazolium trifluoromethylsulfonate ([MIm]TfO) [38], nickel electrodeposition in different PILs such as 2-methylimidazolium lactate ([Hmim][lactate]), 1-ethylimidazolium lactate ([Heim][lactate]), 1-butylimidazolium lactate ([Hbim][lactate]), 2-methylimidazolium glycolate ([Hmim][glycolate]), 1-ethylimidazolium glycolate ([Heim][glycolate]), 1-butylimidazolium glycolate ([Hbim][glycolate]) [39], and triethylammonium trifluoroacetate (TEATFA) [40]. However, most of these studies focus on single metal electrodeposition and further work is required to explore the capabilities of PILs as electrolytes for alloy deposition.

In this work, electrodeposition of amorphous and nanocrystalline Ni-Co alloys in ethylammonium nitrate (EAN), a protic ionic liquid, is reported. The use of EAN in electrodeposition of Ni/Co-based materials is still scarce [41-43]. The electrochemical behavior of Co and Ni ions in EAN have first been studied by voltammetry. Amorphous and nanocrystalline Ni-Co alloy coatings on FTO glass with different thicknesses and composition have been prepared by electrodeposition and characterized using different techniques. These amorphous Ni-Co alloys showed promising behavior with respect to the HER and were compared with the electrochemical behavior of nanocrystalline Ni-Co alloys. With this work, we provide an easy way to tune the composition of an alloy obtained by electrodeposition in IL. Interestingly, reactive materials (towards

electrocatalytic reactions) can be obtained when materials were prepared in an oxygen-free atmosphere.

2. Experimental details

2.1 Chemicals and materials

Ethylamine ($CH_3CH_2NH_2$, 70 wt.% in water, Acros Organics), nitric acid (HNO_3, 68 wt.% in water, AnalaR NORMAPUR), potassium chloride (KCl, 99%, Acros Organics), potassium hydroxide (KOH, 86%, Fisher Scientific), cobalt chloride ($CoCl_2$, 98% purity, Sigma-Aldrich) and nickel chloride ($NiCl_2$, 98%, Sigma-Aldrich) were used as received.

Fluorine-doped Tin Oxide glasses (FTO glass, from Solems, 80 nm thickness) (1.5 × 0.5 × 0.1 cm^3) were used as working electrode after washing in acetone, ethanol, and deionized water, for 15 minutes, respectively.

Nickel wire (99+%) was purchased from Chempur (Germany) and silver wire (99.99%) was from Mateck (Germany).

2.2 Synthesis of the protic ionic liquid

Ethylammonium nitrate (EAN) was prepared by mixing ethylamine and nitric acid with a molar ratio of 1:1. During this process, the nitric acid was added into ethylamine aqueous solution drop by drop under stirring at a controlled temperature (T = -10°C). The purification of EAN was performed by lyophilization (Freeze Dryer -86°C, OPERON CO., LTD.) in order to get EAN with a low water content (below 100 ppm – *vide infra*). The water content in the freshly prepared solvent was titrated using a Karl–

Fisher coulometer (C20, Mettler Toledo) in a glove-box (Concept GP, Jacomex). The salts used for electrochemistry were dried by heating and lyophilization in order to reduce the amount of water in the electrolytes. Solutions of 0.5 M $NiCl_2$, 0.5 M $CoCl_2$, 0.25 M $NiCl_2$ + 0.25 M $CoCl_2$ and 0.375 M $CoCl_2$ + 0.125 M $NiCl_2$ in EAN were prepared by mixing the different compounds under stirring at 70°C for 24 h after weighing. The density and viscosity of the solutions were measured with a densimeter (DSA 5000M, Anton Paar) and a microviscometer (Lovis 2000M, Anton Paar), respectively. The conductivity and pH value of the solutions were measured with a conductimeter (CDM230, Radiometer Analytical) and a pH-meter (PHM250, Radiometer Analytical), respectively.

2.3 Electrochemical measurements and electrodepositions

All the electrochemical measurements were performed using a three-electrode cell and a GAMRY REF600 potentiostat. The electrochemical behavior of Co and Ni was obtained by cyclic voltammetry on a glassy carbon (GC) rotating-disk-electrode (RDE, Pine Research Instrumentation) of 0.2 cm^2 surface area. A platinum grid was used as counter electrode, and the reference electrode consisted of a double junction compartment, in which a silver wire was immersed in the first junction containing a saturated EAN solution of silver nitrate ($AgNO_3$), with a sintered glass at the bottom. The second junction, containing pure EAN, was separated from the first junction in order to prevent ion diffusion from the reference to the electrolyte. For the electrodeposition steps, a 15 mm in diameter nickel ring was used as counter electrode and a FTO glass sheet was used as working electrode (0.5 cm × 0.5 cm). Before

electrochemical measurements, argon was bubbled in the electrolyte for 15 minutes. All the cyclic voltammetry measurements started from the open circuit potential, scanning first towards the cathodic direction and then towards the anodic one, as shown in Figure 1c,d. All alloys electroplating were performed in the glove box to avoid oxygen contamination and limit water ingress.

2.4 Characterizations

The crystal structures of the electrodeposition were characterized by X-ray diffraction (XRD, D8 ADVANCE BRUKER) with a scan rate of 5 degree·min^{-1} from 20° to 80° using the Cu K_α radiation. The surface morphologies of electrodeposition were observed by scanning electron microscopy (SEM, SU-70 HITACHI) with a potential of 5 kV and an energy dispersive X-ray spectroscopy with a potential of 15 kV (EDS, Ultim Max, Oxford Instruments). The grain size and structures of the alloys were determined by transmission electron microscope (TEM, JEM 2011, JEOL) with a potential of 200 kV. The alloys were scratched and separated on the Cu mesh using ethanol. XPS analyses were performed using an Omicron Argus X-ray photoelectron spectrometer, equipped with a monochromated AlKα radiation source (hν = 1486.6 eV) and a 280 W electron beam power. The emission of photoelectrons from the sample was analyzed at a takeoff angle of 45° under ultra-high vacuum conditions ($\leq 10^{-9}$ mBar). Spectra were carried out with a 100 eV pass energy for the survey scan and 20 eV pass energy for the different elements regions. Element peak intensities were corrected by Scofield factors. The peak areas were determined after subtraction of a U 2 Tougaard background. The spectra were fitted using Casa XPS v.2.3.25 software

(Casa Software Ltd, U.K.) and applying a gaussian/lorentzian ratio g/l equal to 70/30 for deconvolution. All XPS samples were transferred directly from the glove box to the XPS instrument after the metal electrodeposition, and measured directly without Ar ion sputtering, in order to learn the real surface state.

2.5 The hydrogen evolution reaction

A three-electrode cell was also used for the electrocatalysis experiments. The FTO glass with the alloy deposit was used as working electrode, a platinum grid and a saturated calomel electrode (SCE) were used as counter and reference electrodes, respectively. The temperature of the electrolyte was controlled at 25°C with a thermostatic bath. A 1.0 M KOH solution was used as electrolyte. Argon was bubbled in the electrolyte for 15 minutes before each experiment and an Ar flux was maintained above the cell for all the duration of the measurement.

The effective active surface area (ECSA) of the samples was evaluated by measuring the interfacial capacitance (C^{σ}) [42].

For an easiest comparison of the results obtained for water splitting, all potentials have been converted with respect to the reversible hydrogen electrode (RHE) at 298 K according to the relationship:

$$E\ (vs.\ \mathrm{RHE}) = E\ (vs.\ \mathrm{SCE}) + 0.0591\ \mathrm{pH} + 0.2412 \qquad (1)$$

3. Results and discussion

3.1 Physicochemical properties of EAN electrolytes

The physicochemical properties of each solution used in this work are presented in

Table 1 as a function of temperature. For each solution with different ion concentrations, the density, the viscosity and the pH values decrease whereas the conductivity increases with increasing temperature. Due to the slight swelling of the IL, the density increases after the addition of $CoCl_2$ or $NiCl_2$ in IL at the same temperature. The viscosity of EAN containing 0.5 M $CoCl_2$ is 37.2 mPa·s at 25°C, which is close to that of pure EAN, 36.4 mPa·s, but significantly lower than the viscosity of EAN containing $NiCl_2$ (Table 1). Similarly, the conductivity of EAN containing 0.5 M $CoCl_2$ is also very close to that of pure EAN for the whole temperature range and is higher than that of EAN containing $NiCl_2$ (Table 1). The pH value of pure EAN at 25°C is 5.61, which is akin to the value in other work [44]. Indeed, the small amount of water (a few hundred ppm) after dissolving ions in the IL is due to the adsorbed water, which is difficult to remove. The variations of the parameters described above are shown in Figure S1.

Table 1. *Physicochemical properties of solutions used in this work.*

Concentration	Temperature (°C)	Density ($g \cdot cm^{-3}$)	Viscosity (mPa·s)	Conductivity ($mS \cdot cm^{-1}$)	pH	Water content (ppm)
Pure EAN	25	1.21040	36.4	21.8	5.61	56
	40	1.20119	22.7	24.9	5.26	
	60	1.18930	13.7	29.0	4.42	
	80	1.17779	9.2	32.7	4.10	
0.5 M $NiCl_2$	25	1.25004	55.0	15.6	4.15	851
	40	1.24016	31.8	18.9	3.35	
	60	1.22733	17.8	23.2	2.49	
	80	1.21484	12.5	28.	2.22	
0.5 M $CoCl_2$	25	1.24308	37.2	21.74	4.11	775
	40	1.23326	22.9	25.8	3.98	
	60	1.22081	13.7	28.3	3.39	
	80	1.20871	10.0	33.1	2.86	
0.25 M $NiCl_2$ + 0.25 M $CoCl_2$	25	1.24233	69.2	19.6	4.20	1034
	40	1.23263	41.5	20.2	3.56	
	60	1.22001	24.2.	25.6	3.02	
	80	1.20785	17.13	30.91	2.77	
0.375 M $CoCl_2$ +0.125 M $NiCl_2$	25	1.24544	48.40	16.93	4.09	780
	40	1.23577	29.09	19.47	3.37	
	60	1.22338	16.93	23.84	2.98	

	80	1.21138	12.13	27.10	2.23

3.2 Electrochemical behavior of EAN with Ni^{2+} and Co^{2+}

EAN is a hydrophilic IL, which means that the experiments performed in air cannot avoid the participation of water and oxygen, although the water content of pure EAN is only 56 ppm. Linear sweep voltammetry and cyclic voltammetry were used to study the electrochemical characteristics of EAN solutions. Figure 1a shows the LSV curves on a glassy carbon (GC) RDE at 1 $mV \cdot s^{-1}$ in pure EAN and for different ion concentrations. The electrochemical window of pure EAN obtained on GC electrode (Figure 1a) is about 2.31 V, which was obtained with a cut-off current density of -0.01 $mA \cdot cm^{-2}$ for the reduction scan and 0.01 $mA \cdot cm^{-2}$ for the oxidation scan. Using these cut-off current densities, the low potential limit of the LSV curve in pure EAN is about -1.2 V/ Ag/Ag^+, which is due to the reduction of EAN. Conversely on the anodic domain, the oxidation of EAN begin at about +1.11 $V/Ag/Ag^+$. A small current plateau is also observed on the anodic scan (starting at about 0.25 $V/Ag/Ag^+$), which was ascribed to the oxidation of a small amount of water present in the IL, which was proved by adjusting the water content, shown in Figure S2a. When Co and Ni salts are added, a shift of the oxidation potentials towards cathodic values is observed (Figure 1). On Figure 1a, the peak at 0.72 $V/Ag/Ag^+$ corresponds to the oxidation reaction of Co^{2+} to Co^{3+}, since it can be increased by increasing the Co^{2+} content. For the cathodic scan, the beginning of electroreduction reaction shifts to -0.94 $V/Ag/Ag^+$ and -1.01 $V/Ag/Ag^+$, which was ascribed to the reduction of Ni^{2+} to Ni and Co^{2+} to Co, respectively.

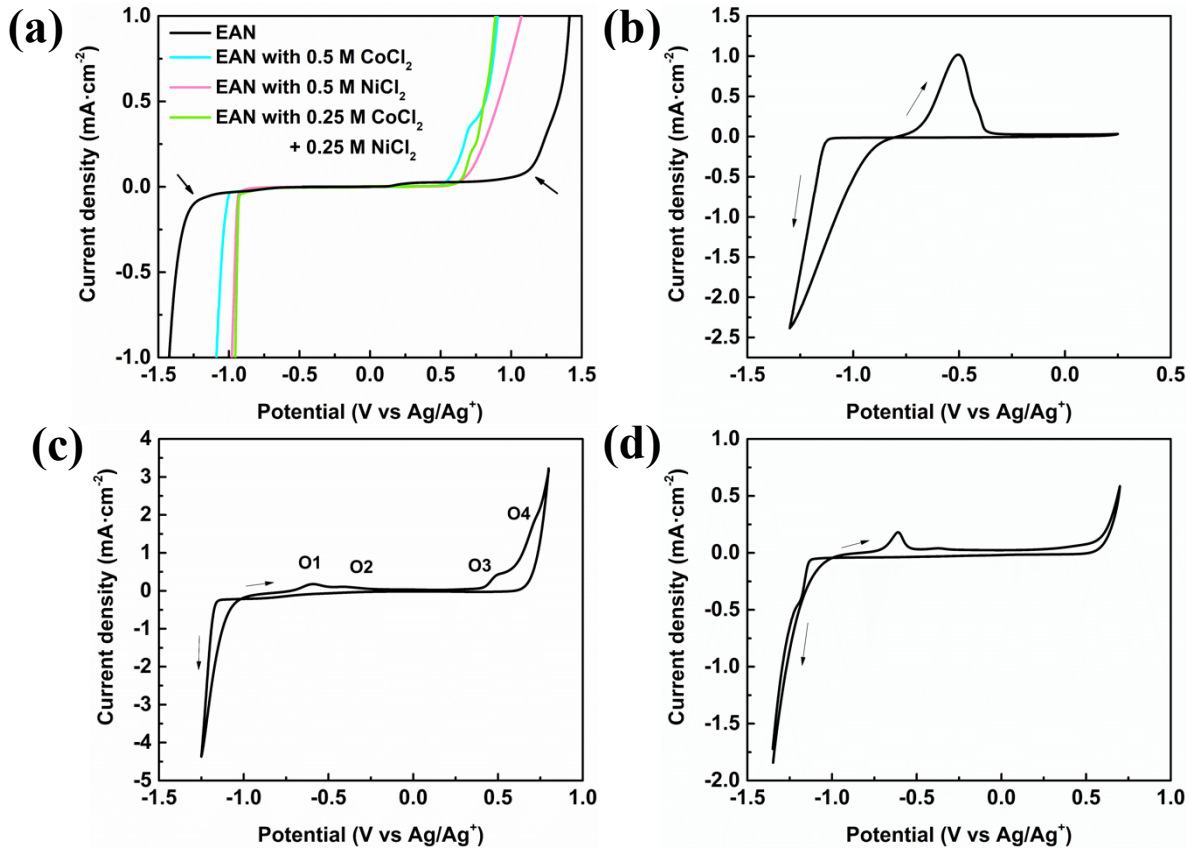

Figure 1. *Electrochemical characterization of EAN with different ions on glassy carbon RDE at 60°C. a) Linear sweep voltammetry curves with or without additional ions at 1 mV s^{-1} and 1000 rpm. Cyclic voltammetry curves, at 50 mV s^{-1}, of EAN with b) 0.5 M $NiCl_2$, c) 0.5 M $CoCl_2$ and d) 0.25 M $NiCl_2$ + 0.25 M $CoCl_2$.*

CV was used to study the reversibility of the electroplating for both metal cations on GC electrode in EAN solution. Although argon was bubbling during the reaction, oxidation of metal deposits (Ni and Co) was difficult to avoid. During the cathodic scan, the shape of the voltammogram is characteristic of a curve usually observed for a metal deposit (Figures 1b-d) with a larger cathodic current during the backward swept. During the anodic scan, Ni dissolves following two successive electron exchange reactions ascribed to Ni to Ni^+ (at about -0.50 V/Ag/Ag^+) and Ni^+ to Ni^{2+} (at about -0.40 V/Ag/Ag^+). A similar oxidation process also occurred for the Co deposit [41]. The O1

and O2 peaks in Figure 1c are ascribed to the oxidation of Co to Co^{+} (at -0.59 V/Ag/Ag^{+}) and Co^{+} to Co^{2+} (at -0.42 V/Ag/Ag^{+}). An additional peak (O3) at about 0.5 V/Ag/Ag^{+} is also observed and corresponds to the oxidation reaction of Co^{2+} to Co^{3+} [43]. At higher overpotentials, the peak O4 is ascribed to the oxidation of Cl^{-}, previously identified with blank experiment (Figure 1a) and proved by changing the concentration of Cl^{-} as shown in Figure S2b, and also in agreement with the literature [45].

Due to the formation of a thin oxide film on the Ni and Co deposits, the reactivity of the electrode during the subsequent cycles is significantly altered. This can be seen and analyzed quantitatively on the chronoamperograms (Figure S3). The charge obtained during the deposition step of the metal is very different from the charge obtained for the re-dissolution step. Then, we can conclude that the electrochemistry of Co and Ni deposited on GC electrode in the air is not fully reversible, and that the electrodeposition of Ni and Co alloys should be performed in an oxygen-free environment.

3.3 Electrodeposition of Ni-Co on FTO glass

Figure 2a shows the polarization curves of the EAN for different ion contents when experiments were performed in a glove box. From these curves, the potential for Ni electrodeposition on FTO glass can be chosen between -0.91 V/Ag/Ag^{+} and -1.3 V/Ag/Ag^{+}, whereas the Co electrodeposition can be performed between -1.05 V/Ag/Ag^{+} and -1.3 V/Ag/Ag^{+}. Thus, pure Ni and pure Co were prepared at potentials of -1.25 V/Ag/Ag^{+} and -1.3 V/Ag/Ag^{+}, respectively, whereas Ni-Co alloys were electrodeposited at different potentials (-1.1, -1.2, and -1.3 V/Ag/Ag^{+}). The

chronoamperometry curves of the electrodeposition process for different potentials, times, and temperatures are shown in Figure 2b. The shape of these curves is similar and the process of electrodeposition can be divided in three parts. For short time, the electric double layer is charged resulting in a sharp cathodic current transient (Figure S4). Then a second variation of the current is observed forming a small bump on the curve which is attributed to the growth of the first crystallites. In a last step, the cathodic current stabilized to a constant value and the system reaches a steady state [46-48].

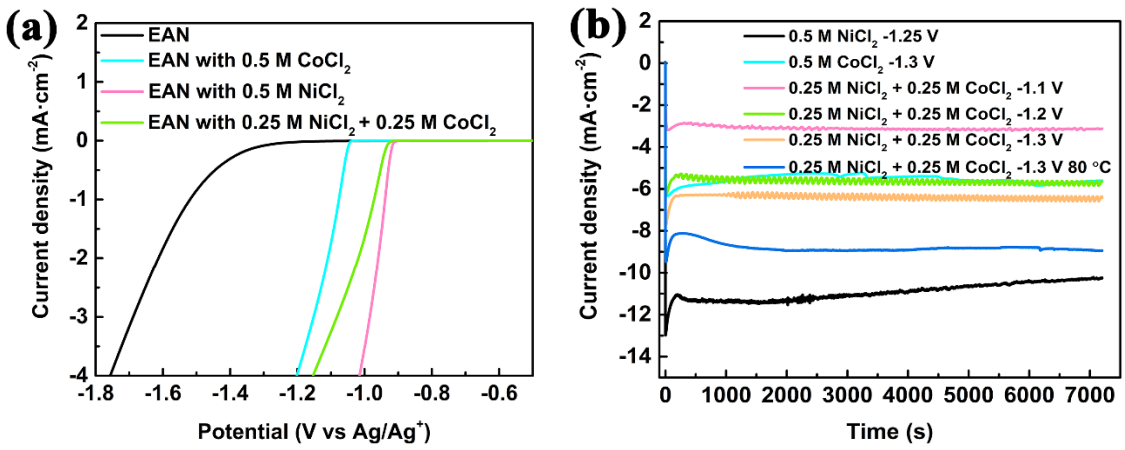

Figure 2. *a) Linear sweep voltammetry curves of EAN with different ions on FTO glass at 60°C performed in glove box. b) Comparison of different current-time curves obtained under various conditions during electrodeposition.*

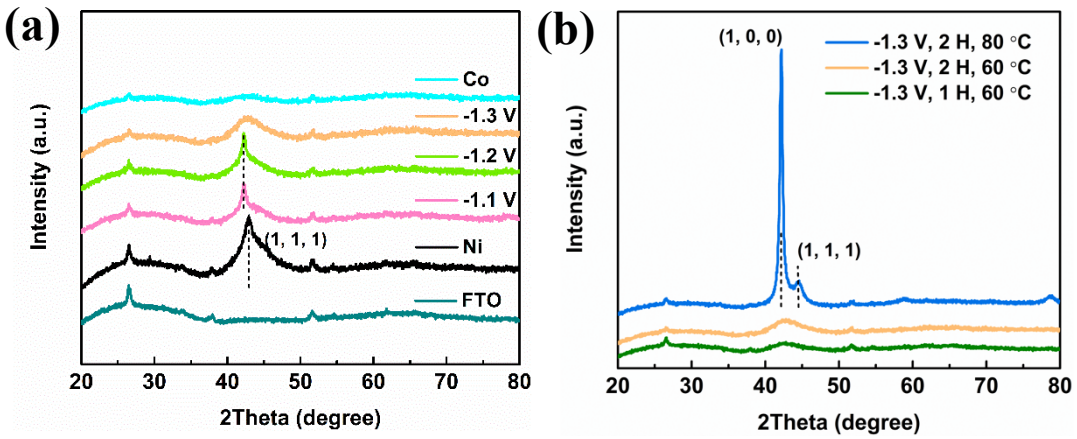

Figure 3. *XRD patterns of different electrodeposited alloys. a) XRD spectra of pure Ni, pure Co and Ni-Co alloys prepared at different potentials on FTO. b) XRD spectra of Ni-Co alloys prepared at different temperatures and times on FTO.*

The XRD spectrum presented in Figure 3a shows that the electrodeposited Ni is nanocrystalline. All the electrodeposited Ni-Co alloys remain in the nanocrystalline state as the electrodeposition potential increases from -1.1 to -1.2 V/Ag/Ag^+, and the (1 1 1) peak moves to lower angle compared with the main moderate amorphous peak, corresponding to the reduction in the lattice size by the doping of Co atoms. When the potential reaches -1.3 V/Ag/Ag^+, the Ni-Co alloy structure changes to amorphous alloy. More negative overpotential results in smaller critical cluster sizes and the cluster forming energy decreases, whereas the cluster formation rate increases, meaning that the nucleation rate during the electrodeposition increases faster than the rate of nuclei growth. As a results, no crystal structure can be observed and an amorphous alloy is obtained [49], as shown in Figure 3b for a 1 hour deposit at 60°C. But the Ni-Co alloy prepared at the same potential for a 1-hour deposit and at a higher temperature (80 °C) is crystallized. Amorphous Co was prepared by electrodeposition at a potential of -1.3

V/Ag/Ag^+, as shown on figure 3a. Amorphous Co thin layer was obtained in the past even by electrodeposition in the presence of thiourea [50]. Here, the presence of IL, and especially the ethylammonium cation can contribute to this morphology.

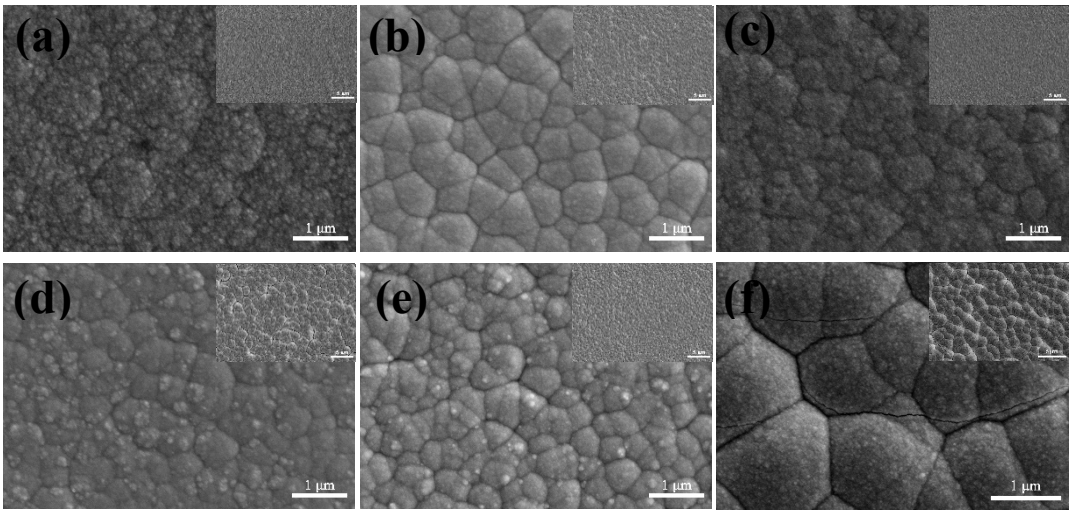

Figure 4. *SEM morphologies of electrodeposited a) Ni, b) Co, and Ni-Co alloys prepared at c) -1.1 V/Ag/Ag^+, d) -1.2 V/Ag/Ag^+, e) -1.3 V/Ag/Ag^+ and f) -1.3 V/Ag/Ag^+ at 80 °C.*

The morphologies of electrodeposited alloys are shown in Figure 4. The alloy composition can be tuned by changing the potential of the deposit, its duration, and the temperature. The different electrodeposition potentials result in similar smooth film on the surface. The surfaces consist of irregular clusters but the nanocrystals and grain boundaries cannot be observed through SEM. Ni-Co alloys deposited at higher temperature, i.e., 80°C, show bigger clusters and obvious cracks, which are due to the expansion of the volume of the thick layer. The elemental analysis performed by EDS is presented in Figure S5. For a given experimental conditions, namely at the same temperature (60°C), ion concentration (0.25 M $NiCl_2$ + 0.25 $CoCl_2$) and the duration of electrodeposition (2 hours), the Co content in the Ni-Co alloys gradually increases when

the electrodeposition potential is shifted toward more cathodic values, from 11 at% to 23 at% and 48 at%, corresponding to a potential of -1.1, -1.2, and -1.3 V/Ag/Ag^+, respectively. Decreasing the electrodeposition time from 2 hours to 1 hour leads to a decrease of the Co content from 48 at% to 36 at%. When the temperature was increased to 80°C, although the amount of deposition on the surface was obviously increased due to kinetic enhancement of the electrochemical reaction, the content of cobalt decreases up to 41 at%. Table 2 summarizes the different alloys prepared according to the experimental conditions. The thickness of the different deposits can be obtained from the analysis of the cross section of each sample by EDS and SEM presented in Figure S6. The average thickness of Ni-Co alloys slightly depends on the electrodeposition potential, varying from 5.1, 7.5, and 6.2 μm for potentials of -1.1, -1.2 and -1.3 V/Ag/Ag^+, respectively. All the samples were washed with an ethanol flow in the same way and duration. Therefore, the error due to the peeling of the top surface during the cleaning process can be ignored. As expected, the thickness of the deposit is proportional to the duration of the electrodeposition, while an increase in temperature also results in an increase of the thickness. Moreover, the mapping of the surfaces and of the cross sections of the sample by EDS clearly indicate that the distribution of Ni and Co elements are uniform. An example of these results is presented in Figure S7 for Ni-Co alloy prepared at -1.3 V/Ag/Ag^+.

In order to better describe the relationship between electrodeposition parameters, phases and composition of the deposit, another composition of the deposition bath was used (0.375 M $CoCl_2$ + 0.125 M $NiCl_2$) at different potential. The XRD spectra obtained

on the deposits are presented in Figure S8. The deposit at -1.2 V/Ag/Ag^+ (C-$Ni_{62.0}Co_{38.0}$) is crystallized and results in a similar atomic ratio to the sample which was prepared at -1.3 V/Ag/Ag^+. Through the data in Table 2, the Co content increases with the electrodeposition potential. An amorphous Ni-Co alloy, A-$Ni_{51.9}Co_{48.1}$, is also formed at a higher potential -1.3 V/Ag/Ag^+. Therefore, the formation of amorphous alloys may be due to high cobalt content or high electrodeposition potential. By adjusting the ionic ratio of the solution (0.375 M $CoCl_2$ + 0.125 M $NiCl_2$), it can be seen that although the cobalt content is increased, the formed alloys are all in crystalline state. This indicates that the formation of amorphous alloy is not linked to the Co content of the alloy, but to the potential applied during the electrodeposition. It can also be seen that the alloy with a higher Co content prepared at -1.3 V/Ag/Ag^+, C-$Ni_{30.9}Co_{69.1}$, shows a nanocrystalline structure but its peak is not as sharp as C-$Ni_{62.0}Co_{38.0}$, which is prepared at a lower potential. The evaluation of the grain size was performed with the Debye-Scherrer equation:

$$D = \frac{K\gamma}{\mathrm{B}\cos\theta} \qquad (2)$$

where D is the mean size of the crystalline, K is the dimensionless shape factor (K = 0.89), γ is the X-ray wavelength, B is the line broadening at half the maximum intensity (FWHM), and θ is Bragg angle. The grain sizes of different crystal alloys are reported in Table 2. The average grain size decreases from 14.8 to 12.0 nm when the potential decreases towards more cathodic values, until obtaining the amorphous alloys at the potential of -1.3 V/Ag/Ag^+. The nano size grains of C-$Ni_{88.7}Co_{11.3}$ can also be measured through TEM, which is around 13 nm (Figure 5b). This value is similar to the one

calculated with the Debye-Scherrer relationship (Table 2), showing that the grain size calculated with Eq. 4 may correspond to the actual grain size. The grains in amorphous alloy A-$Ni_{51.9}Co_{48.1}$ ~~are~~ could be the cobalt oxide and nickel oxide, which ~~were~~ could be formed in the air during the preparation period of TEM measurements, shown through electron diffraction in Figure 5d. For the alloys prepared by electrodeposition from another electrolyte concentration, the change in grain size with the potential also follows the same rule with a decrease of the grain size when the applied electrodeposition potential varies from -1.2 to -1.3 V/Ag/Ag^+.

Table 2. Content of Ni and Co for different alloys prepared in various conditions.

	Potential (V/Ag/Ag^+)	Time (h)	Temperature (℃)	Co (at%)	Ni (at%)	State	Composition	Grain size (nm)
0.5 M $NiCl_2$ + 0.5 M $CoCl_2$	-1.25	2	60	0	100.00	Crystal	C-Ni	16.1
	-1.3	2	60	100.00	0	Amorphous	A-Co	-
0.25 M $CoCl_2$ + 0.25 M $NiCl_2$	-1.1	2	60	11.28	88.72	Crystal	C-$Ni_{88.7}Co_{11.3}$	14.8
	-1.2	2	60	22.82	77.18	Crystal	C-$Ni_{77.2}Co_{22.8}$	12.0
	-1.3	2	60	48.12	51.88	Amorphous	A-$Ni_{51.9}Co_{48.1}$	-
	-1.3	1	60	35.56	64.44	Amorphous	A-$Ni_{64.4}Co_{35.6}$	-
	-1.3	2	80	41.42	58.58	Crystal	C-$Ni_{58.6}Co_{41.4}$	20.5
0.375 M $CoCl_2$ +0.125 M $NiCl_2$	-1.2	2	60	38.00	62.00	Crystal	C-$Ni_{62.0}Co_{38.0}$	29.0
	-1.3	2	60	69.10	30.90	Crystal	C-$Ni_{30.9}Co_{69.1}$	22.2

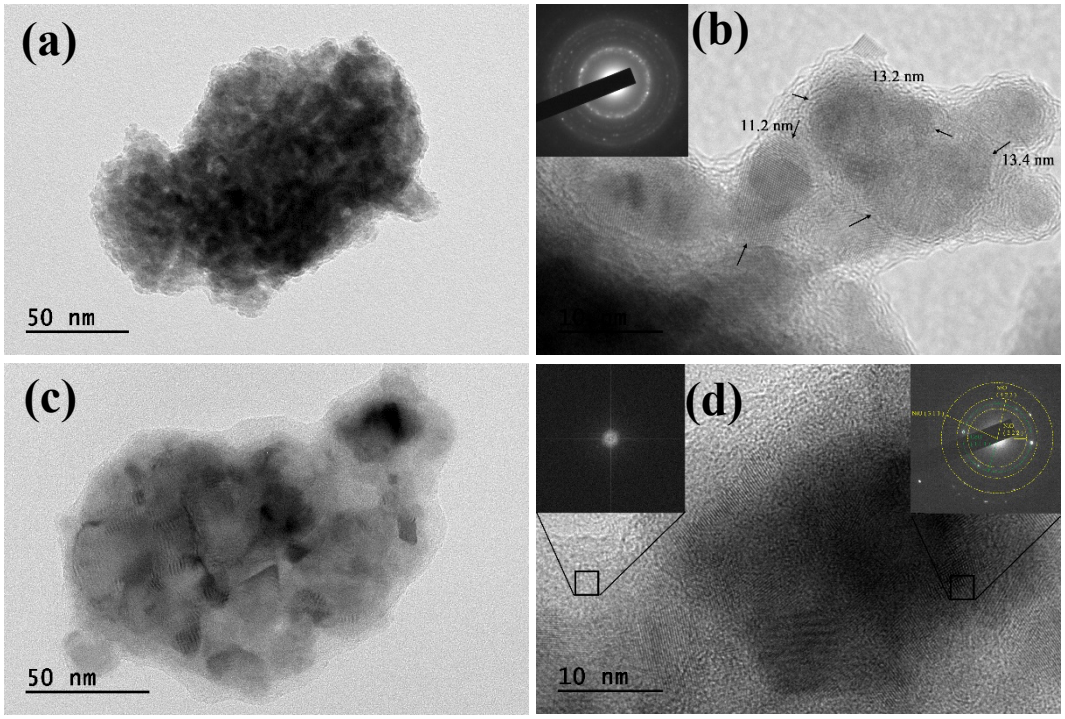

Figure 5. *TEM images of different electrodeposited alloys. a, b) C-$Ni_{88.7}Co_{11.3}$ c,d) A-$Ni_{64.4}Co_{35.6.}$*

XPS analysis was further used to characterize the surface state of different deposits prepared at different potentials. XPS of bonding energy of several compounds of interest are given in table 3. As shown in Figure 6, for deposit performed in Ni-containing electrolytes, a mixture of Ni(0) (852.8 eV), Ni(II) ($NiO/Ni(OH)_2$) (855.5 eV, 855.6 eV is obtained. NiO and $Ni(OH)_2$ originate from the oxidation during sample transfer, which also makes the main peak shifting towards higher level of energy. The oxide can also be identified through TEM in Figure 5b and 5d. The energy of electrons used for performing the XPS analysis is such that the detector can only sense the signal from 10 first nanometers below the surface of the deposit, showing that the oxide film thickness is either smaller than 10 nm or the oxide film does not completely cover the surface. Similarly, for deposit performed from Co-containing electrolytes, a mixture of Co(0) (778.2 eV), Co(II) ($CoO/Co(OH)_2$) (780.6 eV) is also observed. For Ni-Co alloy,

in addition to the oxides and hydroxides, the main peak in Ni 2p and Co 2p spectra for the alloy prepared at -1.1 V/Ag/Ag^+ corresponds to the binding energy of Ni-Co (852.7 eV for Ni 2p and 778.5 eV for Co 2p), showing that the predominant bond in the crystallized Ni-Co alloy is the Ni-Co bond rather than elemental Ni and elemental Co contained in the amorphous Ni-Co alloy shown in Figures 6e and f. These results are in agreement with XRD analysis and TEM measurements. Additionally, nitrate anions remain in the deposit due to the combination of NO_3^- with the alloys at the electrode surface during the electrodeposition process, which can also be observed in the EDS analysis, shown in Figure S5.

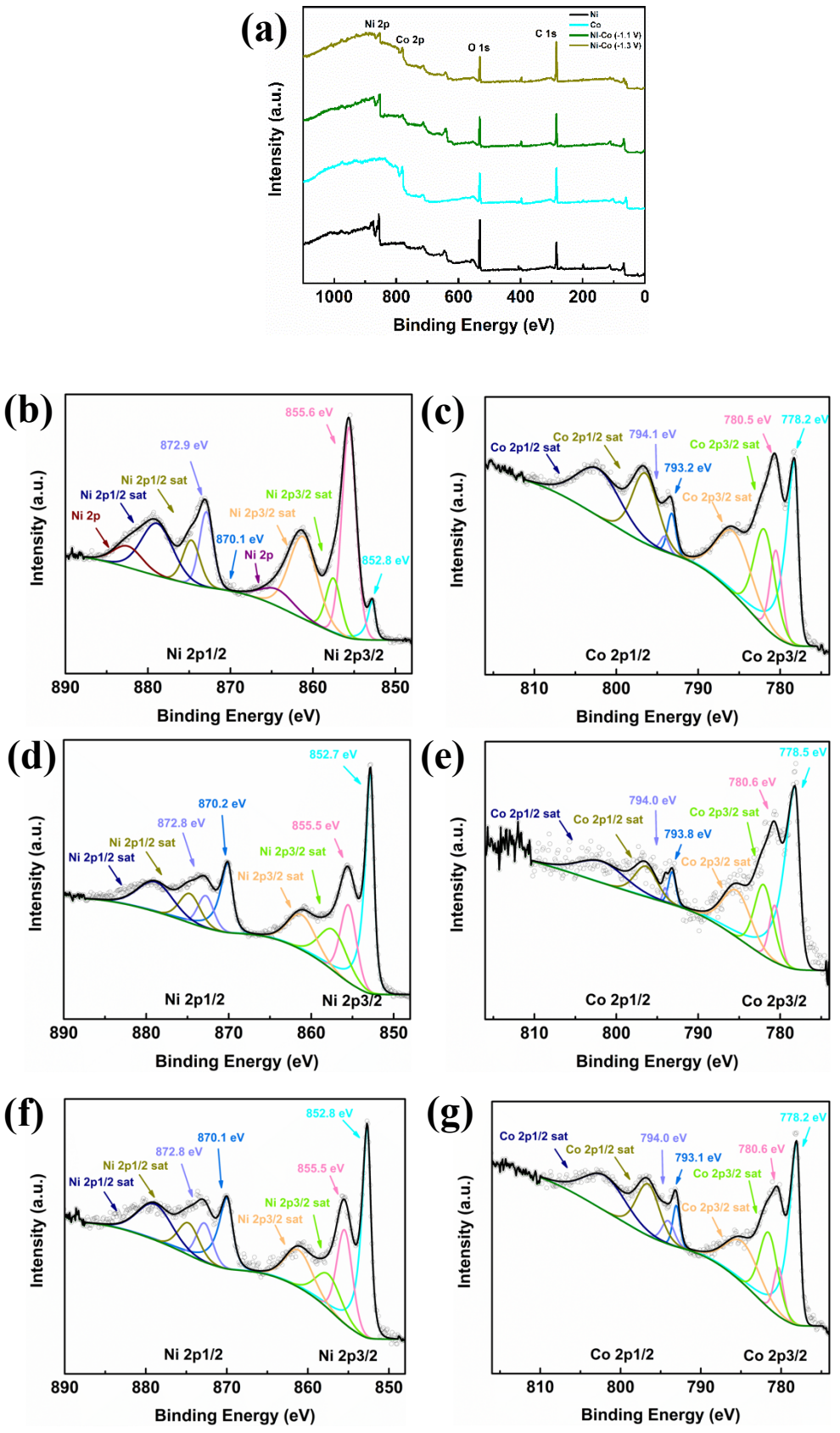

Figure 6. *XPS spectra of different electrodeposited alloys. a) survey b) Ni 2p of deposited Ni, c) Co 2p*

of deposited Co, d) Ni 2p and e) Co 2p of deposited Ni-Co alloys prepared at -1.1 V/Ag/Ag$^+$, f) Ni 2p and g) Co 2p of deposited Ni-Co alloys prepared at -1.3 V/Ag/Ag$^+$.

Table 3. *XPS bonding energy of different compounds [51-54].*

	Ni	Co	$NiO/Ni(OH)_2$	$CoO/Co(OH)_2$	Co-Ni	$(NO_3)^-$	SnO
Ni 2p3/2 (eV)	852.8	-	855.5, 855.6	-	852.7	-	-
Co 2p3/2 (eV)	-	778.2	-	780.5, 780.6	778.5	-	-
O 1s (eV)	-	-	528.9/532.3	529.1/532.5	-	-	530.9, 531.0
N 1s (eV)	-	-	-	-	-	406.7	-

3.4 The electrocatalytic hydrogen evolution reaction of water at Ni-Co alloys

The electrocatalytic properties of these materials have been investigated against the HER by linear sweep voltammetry and cyclic voltammetry in 1 M KOH aqueous solution as shown in Figure 7. The ECSA was evaluated from the determination of the interfacial capacitance (C^{σ}) at different scan rates (Figure S11) at open circuit potential. The variation of the current density as a function of the scan rate for different alloys compositions is shown in Figure 7a. From the slope of these curves, the interfacial capacitance varies from 1.1 mF.cm^{-2} for pure cobalt to 0.12 mF.cm^{-2}. Compared with pure C-Ni, Ni-Co alloys show higher ECSA values, shown in Table 4. The capacitance value of the crystalline C-$Ni_{30.9}Co_{69.1}$ is 0.47 mF·cm^{-2}, which is almost 4 times higher than pure Ni. However, the capacitance values for the different Ni-Co alloys are lower than those of amorphous Co. Such large values may not be ascribed to the double layer capacitance (which is usually in the range of a about 10-50 μF cm^{-2}), but rather to the formation of a thin oxide film on the alloy when immersed in KOH solution, the thickness of which may depend on the alloy composition.

The overpotential are delimited by the potential value for which the current density reaches 10 mA·cm^{-2}. It can be seen from Figure 7b that Ni-Co alloys show lower overpotentials in HER compared with Ni and Co. With the addition of Co, the HER overpotential of different crystalline Ni-Co alloys at 10 mA·cm^{-2} decreases from -0.49 V/RHE to -0.48 V/RHE, -0.42 V/RHE and -0.34 V/RHE, corresponding to Co content of 0 at.%, 11 at.%, 38 at.% and 69 at.%, respectively. For amorphous A-$Ni_{64.4}Co_{35.6}$ and

A-$Ni_{51.9}Co_{48.1}$, the overpotential is -0.30 V/RHE and -0.19 V/RHE, which is lower than overpotentials of C-Ni and A-Co (Figure 7c). Comparing the alloys with similar atomic ratio, amorphous A-$Ni_{51.9}Co_{48.1}$ shows lower overpotential and lower onset potential (-0.19 V/RHE and 0 V/RHE) than crystalline C-$Ni_{58.6}Co_{41.4}$ (-0.46 V/RHE and -0.17 V/RHE). Compared to the ordinary crystalline alloys, the lower HER overpotential of amorphous alloys is due to the synergistic effect of the alloy atoms, the high surface energy of amorphous state and the active center density of amorphous alloys. The amorphous A-$Ni_{51.9}Co_{48.1}$ alloy also shows better value for the overpotential of HER than other works in the literature with the same conditions, like -0.31 V/RHE for Ni-Co nanocomposite and -0.223 V/RHE for nanoporous alloy np-NiFeMoP [55, 56]. It is also lower that than -0.213 V/RHE for Ni-Co alloys with similar element ratio in another work [57]. Moreover, the amorphous alloys also show fast reaction rate, as lower Tafel slope than the crystalline alloys, which is 83.6 $mV \cdot dec^{-1}$, and 71.3 $mV \cdot dec^{-1}$, corresponding to A-$Ni_{64.4}Co_{35.6}$ and A-$Ni_{51.9}Co_{48.1}$. However, it is not an ideal value for HER because of the unstable surface during the reaction. It has been observed that the electrocatalysis is always accompanied by structural rearrangement, possible mineral dissolution, oxidative damage, and physical stress from the gas evolution which render the catalyst physically unstable. Work is under progress for characterizing the stability of these electrodes during long term electrolysis.

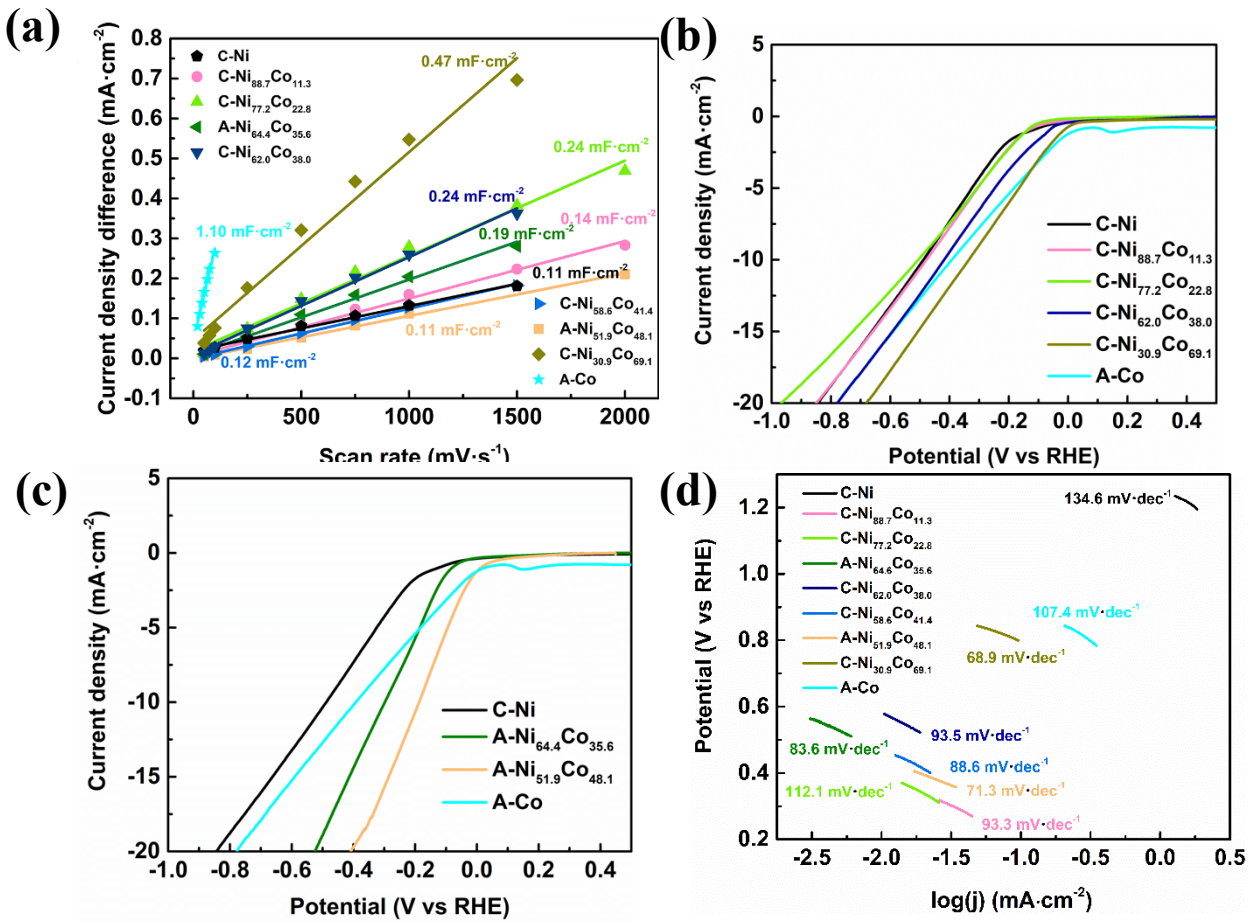

Figure 7. *Electrocatalytic properties of the materials towards the HER for different Ni-Co alloys: a) C^{σ} of different Ni-Co alloys, b) LSV curves of Ni-Co alloys with different atomic ratio at a scan rate of 20 mV/s, c) LSV curves of crystalline Ni-Co alloy and amorphous Ni-Co alloy at a scan rate of 20 mV/s, d) Tafel slopes for different alloys for the HER.*

Table 4. Properties of Ni-Co alloys in 1 M KOH solution towards the HER

	C-Ni	C-Ni$_{88.7}$Co$_{11.3}$	C-Ni$_{77.2}$Co$_{22.8}$	A-Ni$_{64.4}$Co$_{35.6}$	C-Ni$_{62.0}$Co$_{38.0}$	C-Ni$_{58.6}$Co$_{41.4}$	A-Ni$_{51.9}$Co$_{48.1}$	C-Ni$_{30.9}$Co$_{69.1}$	A-Co
C^{σ} (mF·cm^{-2})	0.11	0.14	0.24	0.11	0.19	0.12	0.24	0.47	1.10
OCP (V/RHE)	0.45	0.56	0.57	0.62	0.61	0.58	0.64	0.91	0.91
Onset potential (V vs RHE)	-0.16	-0.13	-0.12	-0.08	-0.08	-0.17	0	-0.01	0 I
Overpotential (V vs RHE)	-0.49	-0.48	-0.51	-0.30	-0.42	-0.46	-0.19	-0.34	-0.40
Tafel slope (mV·dec^{-1})	134.6	93.3	112.1	83.6	93.5	88.6	71.3	68.9	107.4

4. Conclusions

In this work, the electrodeposition of pure Ni, pure Co, and Ni-Co alloys of various

compositions in EAN, a protic ionic liquid, and their properties in HER electrocatalysis were studied. The deposit of Co and Ni as ~~the~~ pure metal on glassy carbon in EAN in the air atmosphere is not a reversible process ~~since it leads~~ leading to the formation of oxides. Nevertheless, we have succeeded in preparing, for the first time in EAN, to our knowledge, pure amorphous Co, nanocrystalline Ni and nanocrystalline/amorphous Ni-Co alloys by electrodeposition on FTO glass in an oxygen-free environment. These electroplated compounds were used as electrocatalysts for HER. The promotion effect of the Co addition on the HER to Ni-based alloys was studied and shown that the better result was obtained with the amorphous alloy, A-$Ni_{51.9}Co_{48.1}$. The amorphous state of the alloy exhibits a lower HER overpotential and faster reaction rate than crystalline alloys with the similar atomic ratio. However, there is still room for improvement in the stability of the deposited materials. This study demonstrates that a protic ionic liquid such as EAN is a good choice for the electrodeposition of Ni-based materials and it opens up a new way for the preparation of Ni/Co-based electrocatalysts, providing an interesting route for tuning the composition of alloys by electrodeposition. Work is currently underway to control the crystallite size and to prepare 3-metal alloys of controlled composition.

4. Acknowledgements

Yuelin XIE was supported by the China Scholarship Council for 3-year Ph.D. study at the Sorbonne Université.

5. Reference

[1] M. Zhao, K. Abe, S.-i. Yamaura, Y. Yamamoto, N. Asao, Fabrication of Pd–Ni–P Metallic Glass Nanoparticles and Their Application as Highly Durable Catalysts in Methanol Electro-oxidation, Chem. Mater., 26 (2014) 1056-1061.

[2] J.K. Norskov, T. Bligaard, A. Logadottir, J.R. Kitchin, J.G. Chen, S. Pandelov, J.K. Norskov, Trends in the exchange current for hydrogen evolution, J. Electrochem. Soc., 152 (2005) J23-J26.

[3] M. Gong, D.-Y. Wang, C.-C. Chen, B.-J. Hwang, H. Dai, A mini review on nickel-based

electrocatalysts for alkaline hydrogen evolution reaction, Nano Research, 9 (2016) 28-46.
[4] A. Karimzadeh, M. Aliofkhazraei, F.C. Walsh, A review of electrodeposited Ni-Co alloy and composite coatings: Microstructure, properties and applications, Surf. Coat. Technol., 372 (2019) 463-498.
[5] X. Cui, M. Chen, R. Xiong, J. Sun, X. Liu, B. Geng, Ultrastable and efficient H2 production via membrane-free hybrid water electrolysis over a bifunctional catalyst of hierarchical Mo–Ni alloy nanoparticles, Journal of Materials Chemistry A, 7 (2019) 16501-16507.
[6] L. Chen, S. Yang, K. Qian, W. Wei, C. Sun, J. Xie, In situ growth of N-doped carbon coated CoNi alloy with graphene decoration for enhanced HER performance, Journal of Energy Chemistry, 29 (2019) 129-135.
[7] S.W. Im, H. Ahn, D.H. Seo, S. Park, S. Choi, W. Ryu, K. Kim, E.S. Park, K.T. Nam, A scalable Al–Ni alloy powder catalyst prepared by metallurgical microstructure control, Journal of Materials Chemistry A, 8 (2020) 11133-11140.
[8] A. Laszczyńska, I. Szczygieł, Electrocatalytic activity for the hydrogen evolution of the electrodeposited Co–Ni–Mo, Co–Ni and Co–Mo alloy coatings, Int. J. Hydrogen Energy, 45 (2020) 508-520.
[9] K. Skibińska, D. Kutyła, A. Kula, M. Gajewska, M.M. Marzec, P. Żabiński, Hydrogen evolution reaction (HER) activity of conical Co–Fe alloy structures and their application as a sensitive and rapid sensor for H2O2 detection, Archives of Civil and Mechanical Engineering, 22 (2022) 76.
[10] C.A.C. Sequeira, D.M.F. Santos, P.S.D. Brito, Electrocatalytic activity of simple and modified Fe–P electrodeposits for hydrogen evolution from alkaline media, Energy, 36 (2011) 847-853.
[11] S.H. Xie, Y.L. Xie, J.J. Kruzic, K.M. Gu, H.P. Yang, Y.M. Deng, X.R. Zeng, The Pivotal Role of Boron in Improving the Azo Dye Degradation of Glassy Fe-based Catalysts, Chemcatchem, 12 (2020) 750-761.
[12] Z. Jia, Y. Zhao, Q. Wang, F. Lyu, X. Tian, S.X. Liang, L.C. Zhang, J. Luan, Q. Wang, L. Sun, T. Yang, B. Shen, Nanoscale Heterogeneities of Non-Noble Iron-Based Metallic Glasses toward Efficient Water Oxidation at Industrial-Level Current Densities, ACS Appl Mater Interfaces, 14 (2022) 10288-10297.
[13] Y. Zhai, X. Ren, J. Yan, S. Liu, High Density and Unit Activity Integrated in Amorphous Catalysts for Electrochemical Water Splitting, Small Structures, 2 (2021) 24.
[14] W.H. Wang, Dynamic relaxations and relaxation-property relationships in metallic glasses, Prog. Mater Sci., 106 (2019) 100561.
[15] K. Nomoto, A.V. Ceguerra, C. Gammer, B. Li, H. Bilal, A. Hohenwarter, B. Gludovatz, J. Eckert, S.P. Ringer, J.J. Kruzic, Medium-range order dictates local hardness in bulk metallic glasses, Mater. Today, 44 (2021) 48-57.
[16] Q. Han, S. Cui, N. Pu, J. Chen, K. Liu, X. Wei, A study on pulse plating amorphous Ni–Mo alloy coating used as HER cathode in alkaline medium, Int. J. Hydrogen Energy, 35 (2010) 5194-5201.
[17] V. Bachvarov, E. Lefterova, R. Rashkov, Electrodeposited NiFeCo and NiFeCoP alloy cathodes for hydrogen evolution reaction in alkaline medium, Int. J. Hydrogen Energy, 41 (2016) 12762-12771.
[18] Y. Ullal, A.C. Hegde, Electrodeposition and electro-catalytic study of nanocrystalline Ni–Fe alloy, Int. J. Hydrogen Energy, 39 (2014) 10485-10492.
[19] Y. Li, X. Zhang, A. Hu, M. Li, Morphological variation of electrodeposited nanostructured Ni-Co alloy electrodes and their property for hydrogen evolution reaction, Int. J. Hydrogen Energy,

43 (2018) 22012-22020.
[20] M. Negem, H. Nady, C.W. Dunnill, Nanocrystalline Ni–Cu Electroplated Alloys Cathodes for Hydrogen Generation in Phosphate-Buffered Neutral Electrolytes, Journal of Bio- and Tribo-Corrosion, 6 (2020).
[21] J. Xie, Y. Xie, Structural Engineering of Electrocatalysts for the Hydrogen Evolution Reaction: Order or Disorder?, ChemCatChem, 7 (2015) 2568-2580.
[22] J.R. McKone, B.F. Sadtler, C.A. Werlang, N.S. Lewis, H.B. Gray, Ni–Mo Nanopowders for Efficient Electrochemical Hydrogen Evolution, ACS Catalysis, 3 (2013) 166-169.
[23] J. Chen, Y. Ling, D. Qu, L. Huang, J. Li, P. Tang, A. He, X. Jin, Y. Zhou, M. Xu, J. Du, Z. Han, Q. Xu, Enhanced electrocatalysis of NiMnIn Heusler alloy films for hydrogen evolution reaction by magnetic field, J. Alloys Compd., 877 (2021).
[24] B. Bayatsarmadi, Y. Zheng, V. Russo, L. Ge, C.S. Casari, S.Z. Qiao, Highly active nickel-cobalt/nanocarbon thin films as efficient water splitting electrodes, Nanoscale, 8 (2016) 18507-18515.
[25] S.J. Gutić, A.Z. Jovanović, A.S. Dobrota, D. Metarapi, L.D. Rafailović, I.A. Pašti, S.V. Mentus, Simple routes for the improvement of hydrogen evolution activity of Ni-Mo catalysts: From sol-gel derived powder catalysts to graphene supported co-electrodeposits, Int. J. Hydrogen Energy, 43 (2018) 16846-16858.
[26] R. Solmaz, A. Döner, G. Kardaş, Preparation, characterization and application of alkaline leached CuNiZn ternary coatings for long-term electrolysis in alkaline solution, Int. J. Hydrogen Energy, 35 (2010) 10045-10049.
[27] S.H. Ahn, S.J. Hwang, S.J. Yoo, I. Choi, H.-J. Kim, J.H. Jang, S.W. Nam, T.-H. Lim, T. Lim, S.-K. Kim, J.J. Kim, Electrodeposited Ni dendrites with high activity and durability for hydrogen evolution reaction in alkaline water electrolysis, J. Mater. Chem., 22 (2012).
[28] J. Wang, H. Shao, S. Ren, A. Hu, M. Li, Fabrication of porous Ni-Co catalytic electrode with high performance in hydrogen evolution reaction, Appl. Surf. Sci., 539 (2021).
[29] X. He, Z. Sun, Q. Zou, J. Yang, L. Wu, Codeposition of Nanocrystalline Co-Ni Catalyst Based on 1-ethyl-3-methylimidazolium Bisulfate and Ethylene Glycol System for Hydrogen Evolution Reaction, J. Electrochem. Soc., 166 (2019) D908-D915.
[30] X. He, Z. Hu, Q. Zou, J. Yang, R. Guo, L. Wu, Co-deposition of Co-Ni alloy catalysts from an ethylene glycol system for the hydrogen evolution reaction, RSC Adv, 13 (2023) 8901-8914.
[31] G. Barati Darband, M. Aliofkhazraei, A.S. Rouhaghdam, Facile electrodeposition of ternary Ni-Fe-Co alloy nanostructure as a binder free, cost-effective and durable electrocatalyst for high-performance overall water splitting, J. Colloid Interface Sci., 547 (2019) 407-420.
[32] H. Zhou, C. Peng, S. Jiao, W. Zeng, J. Chen, Y. Kuang, Electrodeposition of nanoscaled nickel in a reverse microemulsion, Electrochem. Commun., 8 (2006) 1142-1146.
[33] G.B. Darband, M. Aliofkhazraei, A.S. Rouhaghdam, M.A. Kiani, Three-dimensional Ni-Co alloy hierarchical nanostructure as efficient non-noble-metal electrocatalyst for hydrogen evolution reaction, Appl. Surf. Sci., 465 (2019) 846-862.
[34] F. Ganci, V. Cusumano, P. Livreri, G. Aiello, C. Sunseri, R. Inguanta, Nanostructured Ni–Co alloy electrodes for both hydrogen and oxygen evolution reaction in alkaline electrolyzer, Int. J. Hydrogen Energy, 46 (2021) 10082-10092.
[35] A. Maurya, S. Suman, A. Bhardwaj, L. Mohapatra, A.K. Kushwaha, Substrate Dependent Electrodeposition of Ni–Co Alloy for Efficient Hydrogen Evolution Reaction, Electrocatalysis, 14

(2022) 68-77.
[36] A.P. Abbott, K.J. McKenzie, Application of ionic liquids to the electrodeposition of metals, Phys. Chem. Chem. Phys., 8 (2006) 4265-4279.
[37] B.H.R. Suryanto, C.A. Gunawan, X. Lu, C. Zhao, Tuning the electrodeposition parameters of silver to yield micro/nano structures from room temperature protic ionic liquids, Electrochim. Acta, 81 (2012) 98-105.
[38] Z. Liu, S.Z. El Abedin, F. Endres, Dissolution of zinc oxide in a protic ionic liquid with the 1-methylimidazolium cation and electrodeposition of zinc from ZnO/ionic liquid and ZnO/ionic liquid–water mixtures, Electrochem. Commun., 58 (2015) 46-50.
[39] B. Meenatchi, V. Renuga, A. Manikandan, Electrodeposition of Nickel on Glassy Carbon Electrode from Protic Ionic Liquids with Imidazolium Cation, Journal of Inorganic and Organometallic Polymers and Materials, 26 (2016) 423-430.
[40] D. Saranya, D. Velayutham, V. Suryanarayanan, Electrodeposition of Ni–Cu alloys from a protic ionic liquid medium-voltammetric and surface morphologic studies, J. Electroanal. Chem., 734 (2014) 70-78.
[41] M. Asnavandi, C. Zhao, Hydrogen Bubble-Assisted Electrodeposition of Metal Nanoparticles from Protic Ionic Liquids for Electrocatalysis, ACS Sustainable Chemistry & Engineering, 5 (2017) 85-89.
[42] L. Wu, J.P. Hofmann, Comparing the Intrinsic HER Activity of Transition Metal Dichalcogenides: Pitfalls and Suggestions, ACS Energy Letters, 6 (2021) 2619-2625.
[43] B.H.R. Suryanto, X. Lu, H.M. Chan, C. Zhao, Controlled electrodeposition of cobalt oxides from protic ionic liquids for electrocatalytic water oxidation, RSC Advances, 3 (2013).
[44] R. Kanzaki, K. Uchida, S. Hara, Y. Umebayashi, S.-i. Ishiguro, S. Nomura, Acid–Base Property of Ethylammonium Nitrate Ionic Liquid Directly Obtained Using Ion-selective Field Effect Transistor Electrode, Chem. Lett., 36 (2007) 684-685.
[45] A. Gupta, C. Srivastava, Nucleation and growth mechanism of tin electrodeposition on graphene oxide: A kinetic, thermodynamic and microscopic study, J. Electroanal. Chem., 861 (2020).
[46] Z. Feng, L. Wang, D. Li, Q. Sun, P. Lu, P. Xing, M. An, Electrodeposition of Ni-Se in a chloride electrolyte: An insight of diffusion and nucleation mechanisms, J. Electroanal. Chem., 847 (2019).
[47] C. Zhao, D.R. MacFarlane, A.M. Bond, Modified Thermodynamics in Ionic Liquids for Controlled Electrocrystallization of Nanocubes, Nanowires, and Crystalline Thin Films of Silver−Tetracyanoquinodimethane, Journal of the American Chemical Society, 131 (2009) 16195-16205.
[48] B. Scharifker, G. Hills, Theoretical and experimental studies of multiple nucleation, Electrochim. Acta, 28 (1983) 879-889.
[49] C. Guo, Y. Fang, B. Wu, S. Lan, G. Peng, X.-l. Wang, H. Hahn, H. Gleiter, T. Feng, Ni-P nanoglass prepared by multi-phase pulsed electrodeposition, Materials Research Letters, 5 (2017) 293-299.
[50] J. García-Torres, E. Gómez, E. Vallés, Modulation of magnetic and structural properties of cobalt thin films by means of electrodeposition, J. Appl. Electrochem., 39 (2009) 233-240.
[51] M.C. Biesinger, B.P. Payne, L.W.M. Lau, A. Gerson, R.S.C. Smart, X-ray photoelectron spectroscopic chemical state quantification of mixed nickel metal, oxide and hydroxide systems, Surf. Interface Anal., 41 (2009) 324-332.
[52] M.C. Biesinger, B.P. Payne, A.P. Grosvenor, L.W.M. Lau, A.R. Gerson, R.S.C. Smart, Resolving surface chemical states in XPS analysis of first row transition metals, oxides and hydroxides: Cr, Mn,

Fe, Co and Ni, Appl. Surf. Sci., 257 (2011) 2717-2730.
[53] N.H. Turner, A.M. Single, Determination of peak positions and areas from wide-scan XPS spectra, Surf. Interface Anal., 15 (1990) 215-222.
[54] R.O. Ansell, T. Dickinson, A.F. Povey, P.M.A. Sherwood, Quantitative use of the angular variation technique in studies of tin by X-ray photoelectron spectroscopy, J. Electron. Spectrosc. Relat. Phenom., 11 (1977) 301-313.
[55] H. Qian, K. Li, X. Mu, J. Zou, S. Xie, X. Xiong, X. Zeng, Nanoporous NiFeMoP alloy as a bifunctional catalyst for overall water splitting, Int. J. Hydrogen Energy, 45 (2020) 16447-16457.
[56] A.E.G.B. Gorospe, M.D.L. Balela, Ni-Co nanocomposites deposited on carbon fiber paper as an electrocatalyst towards hydrogen evolution reaction, Materials Today: Proceedings, 22 (2020) 255-261.
[57] T. Sun, J. Cao, J. Dong, H. Du, H. Zhang, J. Chen, L. Xu, Ordered mesoporous Ni Co alloys for highly efficient electrocatalytic hydrogen evolution reaction, Int. J. Hydrogen Energy, 42 (2017) 6637-6645.